

One photon simultaneously excites two atoms in a ultrastrongly coupled light-matter system

A. Tomonaga,^{1,2,*} R. Stassi,^{3,4} H. Mukai,^{1,2} F. Nori,^{2,4,5} F. Yoshihara,^{1,6} and J. S. Tsai^{1,2,†}

¹*Department of Physics, Tokyo University of Science, Shinjuku, Tokyo 162-0825, Japan*

²*Center for Quantum Computing, RIKEN, Wakoshi, Saitama 351-0198, Japan*

³*Dipartimento di Scienze Matematiche e Informatiche,*

Scienze Fisiche e Scienze della Terra, Università di Messina, I-98166 Messina, Italy

⁴*Theoretical Quantum Physics Laboratory, Cluster for Pioneering Research, RIKEN, Wakoshi, Saitama 351-0198, Japan*

⁵*Physics Department, The University of Michigan, Ann Arbor, Michigan 48109-1040, USA.*

⁶*Advanced ICT Research Institute, National Institute of Information and Communications Technology, Koganei, Tokyo 184-8795, Japan*

We experimentally investigate a superconducting circuit composed of two flux qubits ultrastrongly coupled to a common LC resonator. Owing to the large anharmonicity of the flux qubits, the system can be correctly described by a generalized Dicke Hamiltonian containing spin-spin interaction terms. In the experimentally measured spectrum, an avoided level crossing provides evidence of the exotic interaction that allows the *simultaneous* excitation of *two* artificial atoms by absorbing *one* photon from the resonator. This multi-atom ultrastrongly coupled system opens the door to studying nonlinear optics where the number of excitations is not conserved. This enables novel processes for quantum-information processing tasks on a chip.

Introduction

Superconducting circuits provide a versatile and flexible platform for modeling various quantum systems [1–6]. In this platform, artificial atoms can be designed to have tailored energy transitions and controllable interactions with microwave photons [2]. Moreover, superconducting circuits also became one of the main platforms for scalable quantum information processing and quantum simulation [2–6].

Taking advantage of the high electromagnetic field in a one-dimensional resonator and the huge dipole moment of artificial atoms, these systems achieve a stronger light-matter interaction than the bare atomic or resonator frequencies [7–13]. This ultrastrong (deep-strong) interaction might lead to promising applications, such as high-speed and high-efficiency quantum information processing devices [14–19]. In this coupling regime, several unique physical phenomena have been predicted, and now some of these have been realized experimentally. Important theoretical predictions are, for example, the observation of quantum vacuum radiation and entanglement in the ground state [20–24]. Especially, the observation of induced parity symmetry breaking of an ancillary artificial atom was also demonstrated [25]. In Ref. 25, it is shown that, when is broken the parity symmetry is broken in an atom-light system that is deep in the ultrastrong coupling regime, the light field acquires a coherence in the ground state that induces symmetry breaking in an ancillary flux qubit weakly coupled to the same field [26].

In the ultrastrong coupling regime, one of the most fascinating theoretical predictions is, when the parity symmetry is broken [27–29], one of the most fascinating is that one photon can simultaneously excite two atoms [30, 31]. Similarly to Rabi oscillations, this process, which is mediated by virtual excitations, is a coherent and unitary process and the atoms can jointly emit one photon [29, 30]. The reverse phenomenon, i.e., two photon excitation of an atom or molecule, has been adopted for specific spectroscopic instruments [32, 33]. Likewise, we believe that the two-atom excitation process can open the door to new applications.

We experimentally investigate a circuit composed of two flux qubits ultrastrongly coupled to a common LC resonator. Flux qubits, which form the artificial atoms, share the same inductor with the LC resonator; as a consequence, they interact with each other. This system is described by the Dicke Hamiltonian generalized to include atomic longitudinal couplings and the spin-spin interaction term.

Away from the flux qubit optimal point, where the parity symmetry of the system is broken, in the experimentally measured spectrum, we observe an energy-level anti-crossing, which indicates hybridization between the bare states $|gg\rangle$ and $|ee\rangle$, where $g(e)$ and 0 respectively indicate the atomic ground (excited) and zero photon states. This is the fingerprint of the interaction that allows *one* photon to *simultaneously* excite *two* atoms and the reverse process. When the system is set up in the one-photon state, the artificial atoms and the resonator can exchange excitations in a Rabi-like oscillation.

Since the atom–light and atom–atom interactions are very strong, the atomic states should be strongly hybridized with each other, and should not be possible to clearly observe the effect of “one photon exciting two atoms”. However, the direct atom–atom interaction partially suppress the atom–light interaction. Moreover, de-

* akiyoshi.tomonaga@aist.go.jp; Current affiliation: National Institute of Advanced Industrial Science and Technology (AIST), Tsukuba, Ibaraki 305-8563, Japan

† tsai@riken.jp

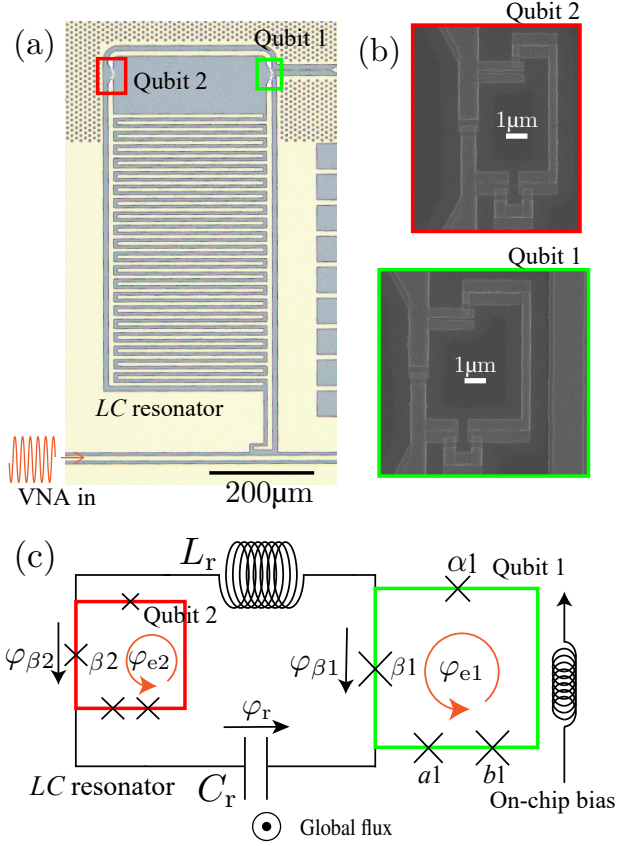


FIG. 1. (a) Optical microscope image of the measured sample. The sample holder has a coil to bias a uniform magnetic field from the back surface of the chip. Qubit 1 has a local bias line that changes the magnetic flux of the qubit loop. The spectrum is measured using a vector network analyzer (VNA) for probing and reading from the transmission line shown below the circuit. (b) SEM images of qubits 1 and 2. The design parameters of both qubit junctions are the same. (c) Equivalent circuit diagram of the sample.

pending on the phase of the longitudinal interaction, the light and matter decouple. Therefore, the spectrum is asymmetric with respect to the sign of the flux bias, and the one photon exciting two atoms effect is clearly observable.

Device

Figure 1(a) shows an optical microscope image of the artificial-atom-resonator circuit. The LC resonator is composed of an interdigital capacitor and line inductance made of a superconducting thin film [34, 35]. The two flux qubits are inductively coupled to the LC resonator via a Josephson junction [Fig. 1(b)], which increases the couplings to the ultrastrong regime. The energies of the flux qubits [36] can be changed applying an external magnetic flux to the loop from a global coil and using an on-

chip bias line. Figure 1(c) shows the equivalent circuit with lumped elements and Josephson junctions.

The Hamiltonian of the entire system is [37–39]

$$\hat{\mathcal{H}}_{\text{tot}} = \hat{\mathcal{H}}_{q1} + \hat{\mathcal{H}}_{q2} + \hat{\mathcal{H}}_r + \hat{\mathcal{H}}_{\text{int}}, \quad (1)$$

where $\hat{\mathcal{H}}_{qk}$ ($k = 1, 2$), $\hat{\mathcal{H}}_r$, and $\hat{\mathcal{H}}_{\text{int}}$ represent the qubits, resonator, and atom-resonator plus atom-atom couplings, respectively. The Hamiltonian of the resonator is $\hat{\mathcal{H}}_r = \hbar\omega_r(\hat{a}^\dagger\hat{a} + 1/2)$, where $\omega_r \equiv 1/\sqrt{L_r C_r}$ is the resonance frequency, $\hat{a} \equiv (\hat{\phi}_r - iZ_r\hat{q}_r)/\sqrt{2\hbar Z_r}$ is the annihilation operator, $\hat{a}^\dagger \equiv (\hat{\phi}_r + iZ_r\hat{q}_r)/\sqrt{2\hbar Z_r}$ is the creation operator, $Z_r = \sqrt{L_r/C_r}$ is the characteristic impedance of the LC resonator, and \hat{q}_r is the conjugate variable of $\hat{\phi}_r = \Phi_0\hat{\varphi}_r$. The Hamiltonian of the k -th artificial atom is defined as

$$\hat{\mathcal{H}}_{qk} \equiv 4E_c\hat{\mathbf{q}}_k^T\mathbf{M}_k^{-1}\hat{\mathbf{q}}_k + E_{Lr}\hat{\varphi}_{\beta k}^2 + \hat{\mathcal{U}}_{Jk}, \quad (2)$$

where E_c is the charging energy of the Josephson junction, \mathbf{M}_k is the normalized mass matrix, $E_{Lr} = \Phi_0^2/(2L_r)$, and $\hat{\mathcal{U}}_{Jk}$ is the qubit potential energy of Josephson junctions:

$$\hat{\mathcal{U}}_{Jk}(\hat{\varphi}_{ek}) = -E_J[\beta_k \cos(\hat{\varphi}_{\beta k}) + \cos(\hat{\varphi}_{ak}) + \cos(\hat{\varphi}_{bk}) + \alpha_k \cos(\varphi_{ek} - \hat{\varphi}_{ak} - \hat{\varphi}_{bk} - \hat{\varphi}_{\beta k})]. \quad (3)$$

Here, E_J is the current energy of the Josephson junction, and φ_{ek} represents the external flux for the loop of each atom. The interaction Hamiltonian

$$\hat{\mathcal{H}}_{\text{int}} = -E_{Lr}(\hat{\varphi}_{\beta 1}\hat{\varphi}_r - \hat{\varphi}_{\beta 2}\hat{\varphi}_r + \hat{\varphi}_{\beta 1}\hat{\varphi}_{\beta 2}) \quad (4)$$

is obtained from the boundary condition (Kirchhoff's voltage law) of the loop forming the resonator with elements L_r and C_r .

By approximating each atom as a two-level system [40], on the basis of persistent currents of the superconducting loop, we obtain the total Hamiltonian in Eq. (1) as

$$\hat{\mathcal{H}}_{\text{tot}}/\hbar \simeq \omega_r\hat{a}^\dagger\hat{a} + \frac{\varepsilon_1}{2}\hat{\sigma}_{z1} + \frac{\Delta_1}{2}\hat{\sigma}_{x1} + \frac{\varepsilon_2}{2}\hat{\sigma}_{z2} + \frac{\Delta_2}{2}\hat{\sigma}_{x2} - (g_1\hat{\sigma}_{z1} - g_2\hat{\sigma}_{z2})(\hat{a}^\dagger + \hat{a}) - \frac{2g_1g_2}{\omega_r}\hat{\sigma}_{z1}\hat{\sigma}_{z2}, \quad (5)$$

where ε_k is the persistent current energy of each qubit, Δ_k is the qubit energy gap when $\varepsilon_k = 0$, while $\hat{\sigma}_{zk}$ and $\hat{\sigma}_{xk}$ are the Pauli matrices for the k -th qubit. We define $\varepsilon_k > 0$ when the qubit current flows anticlockwise and vice versa.

After a unitary transformation that diagonalizes the atomic Hamiltonians $\hat{\mathcal{H}}_{qk}$, we obtain a generalized Dicke Hamiltonian [41] with the spin-spin interaction:

$$\hat{\mathcal{H}}_{\text{tot}}/\hbar \simeq \omega_r\hat{a}^\dagger\hat{a} + \frac{\omega_{q1}}{2}\hat{\sigma}_{z1} + \frac{\omega_{q2}}{2}\hat{\sigma}_{z2} - (g_1\hat{\Lambda}_1 - g_2\hat{\Lambda}_2)(\hat{a}^\dagger + \hat{a}) - \frac{2g_1g_2}{\omega_r}\hat{\Lambda}_1\hat{\Lambda}_2, \quad (6)$$

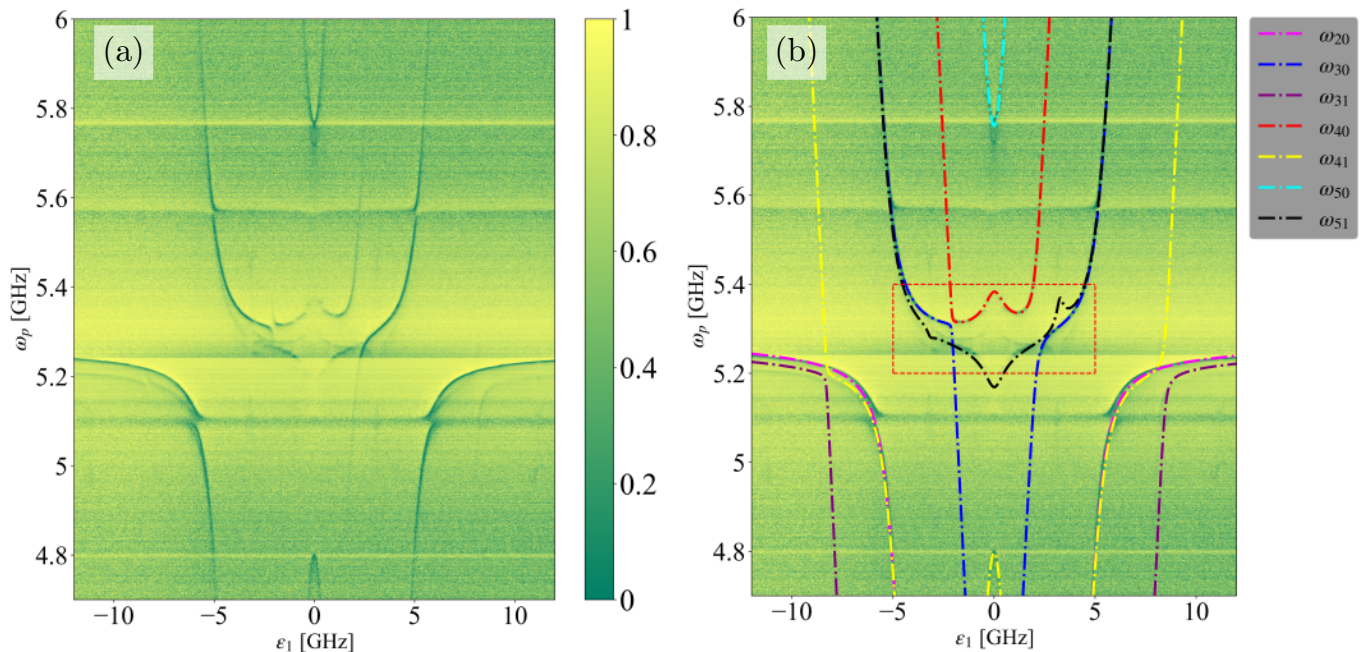


FIG. 2. Pump frequency ω_p from the VNA versus the persistent current energy ε_1 of qubit 1. (a) Raw data of the observed single-tone spectrum of the sample shown in Fig. 1. (b) Observed single-tone spectrum with fitted curves corresponding to the state transition frequencies ω_{ij} between the i -th and j -th eigenstates of Hamiltonian (6). The fit parameters are $g_1/2\pi = 3.31$, $g_2/2\pi = 3.41$, $\Delta_{q1}/2\pi = 1.35$, $\Delta_{q2}/2\pi = 1.26$, $\omega_r/2\pi = 5.14$, and $\varepsilon_2/2\pi = -3.21$ GHz. Note that ω_{31} and ω_{51} are not used for fitting because those signals were too weak, but the curves of ω_{31} and ω_{51} still reproduce well the experimental results. Around 5.09 GHz and 5.57 GHz can be seen parasitic modes, which originate from, for example, sample ground planes and/or the measurement environment; this includes the sample holder and microwave components coupled to the system.

where $\omega_{qk} = \text{sgn}(\varepsilon_k)(\varepsilon_k^2 + \Delta_k^2)^{1/2}$ is the qubit frequency and $\hat{\Lambda}_k = (\cos\theta_k \hat{\sigma}_{xk} + \sin\theta_k \hat{\sigma}_{zk})$ gives the direction of the interaction, with $\theta_k \simeq -\arctan(\Delta_k/\varepsilon_k)$ (details in Appendix A). For $\theta_k = 0$ ($\varepsilon_k = 0$) the interaction is transverse. When $\theta_k \neq 0$, the interaction has a longitudinal component and the one photon exciting two atoms effect is allowed.

Results

Energy spectrum

Figure 2(a) shows the raw data of the measured spectrum as a function of the persistent current energy ε_1 of qubit 1, after fixing the value of $\varepsilon_2/2\pi$ at -3.21 GHz when $\varepsilon_1 = 0$. In Fig. 2(b) the spectrum is fitted with the numerically calculated transition frequencies ω_{ij} between the i -th and j -th eigenstates of the total Hamiltonian $\hat{\mathcal{H}}_{\text{tot}}$. The persistent current energy for qubit 2 and the resonator frequency are affected by the external magnetic flux applied to qubit 1 [8]. Thus, to derive the transitions frequencies ω_{ij} , in Eq. (5), we substitute $\varepsilon_2 \rightarrow \varepsilon_2 + A\varepsilon_1$ and $\omega_r \rightarrow \omega_r(1 + B_{\pm}\varepsilon_1)$, where A and B_{\pm} are fitting parameters. Because the spectrum is asymmetric with respect to the sign of ε_1 , we use two different values for B_{\pm} , where B_+ is used when $\varepsilon_1 \geq 0$ and vice

versa. From the fitting, we obtain $A = -9.10 \times 10^{-3}$, $B_- = 1.13 \times 10^{-3}$, and $B_+ = 0.79 \times 10^{-3}$. To calculate the spectrum, we used the quantum toolbox in Python (QuTip) [42, 43].

Flux qubits 1 and 2 are almost identical except for the loop size; consequently, they have similar fitted parameters, i.e., $\Delta_{q1} = 0.26 \omega_r$ and $\Delta_{q2} = 0.25 \omega_r$. We find atom-resonator couplings rates of $g_1/\omega_r = 0.64$ and $g_2/\omega_r = 0.66$, indicating that the artificial atoms are ultrastrongly coupled with the resonator.

Observing ω_{30} (blue curve) and ω_{40} (red curve) in Figs. 2(b) and especially 3(a), it is possible to notice that the spectrum is asymmetric with respect to the sign of ε_1 . This occurs due to the presence of atom-light longitudinal interactions when two or more qubits are coupled to the same cavity mode [44]. Assuming that there are only longitudinal couplings, the atomic states are associated to photonic coherent states. However, if $\varepsilon_1 > 0$, the atomic and photonic states are decoupled if $M = m_1 - m_2 = 0$, where $m_k = \pm 1$ is the eigenstate of σ_{zk} (details in Appendix B). If $\varepsilon_1 < 0$, the atomic and photonic states are decoupled if $M = -m_1 - m_2 = 0$. In our experimental setup we have both longitudinal and transverse couplings; the presence of the longitudinal components justifies the asymmetry in Fig. 2.

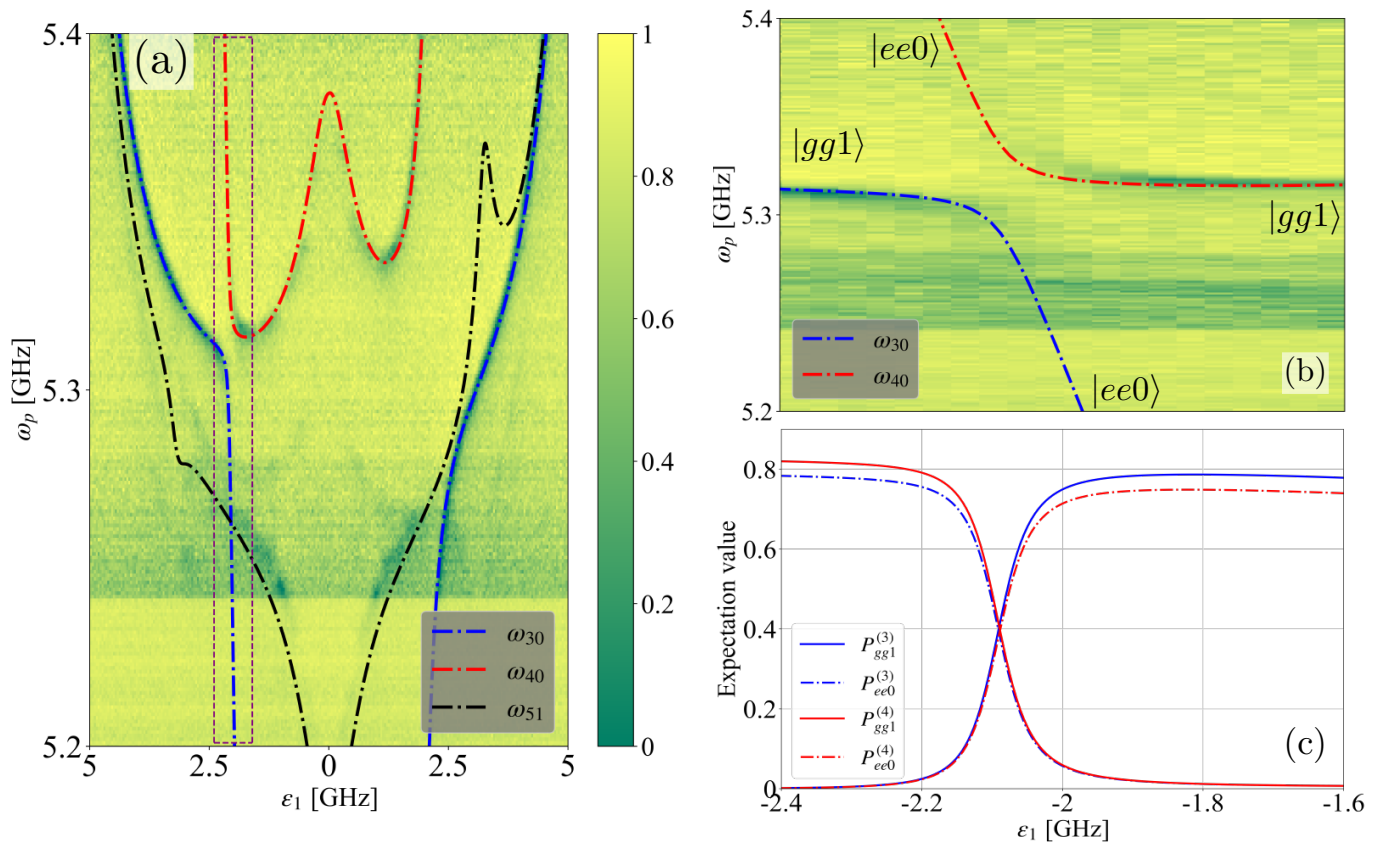


FIG. 3. (a) Enlarged view of the central part of the spectrum in Fig. 2(b) with fitting curve. The fitting reproduces the spectrum well. (b) Enlarged image of the anticrossing between ω_{30} and ω_{40} . (c) Projection of $|gg1\rangle$ and $|ee0\rangle$ bare states to the third and fourth eigenstates calculated using the fitting parameters and Hamiltonian in Eq. (6).

One photon simultaneously excites two atoms

We indicate with $|\psi_i\rangle$ the eigenstate of the system Hamiltonian \hat{H}_{tot} with eigenenergies $\hbar\omega_{i0}$. The terms $\omega_{qi}\hat{\sigma}_{zi}/2$ in Eq. (6) define the ground $|g\rangle$ and excited $|e\rangle$ atomic bare states.

In Fig. 3(a), which is an enlarged view of the red dashed rectangle in Fig. 2(b), the white arrow indicates the anticrossing between the eigenstates $|\psi_3\rangle$ and $|\psi_4\rangle$, with eigenfrequencies ω_{30} and ω_{40} . In correspondence of the anticrossing [see Fig. 3(b)], we numerically calculate the projection $P_j^{(i)} \equiv |\langle\psi_i|j\rangle|^2$ of the third and fourth eigenstates $|\psi_i\rangle$ ($i = 3, 4$) on the bare states $|j\rangle = \{|gg1\rangle, |ee0\rangle\}$ as a function of ε_1 . Figure 3(c) shows that, at the anticrossing, the third and fourth eigenstates are approximate symmetric and asymmetric superpositions of $|gg1\rangle$ and $|ee0\rangle$. Considering also that the sum of the bare qubit frequencies are nearly equal to the bare resonator frequency, $\omega_{q1} + \omega_{q2} \simeq \omega_r$, the anticrossing is the signature of the one photon exciting two atoms effect. Half of the minimum split between ω_{30} and ω_{40} in the spectrum gives the effective coupling between $|gg1\rangle$ and $|ee0\rangle$, that is 22 MHz (details in Appendix C).

With respect to the theoretical prediction in Ref. 30, our system has a much larger coupling. This implies that the system eigenstates should have a strong dressing, and in principle we could not observe a clean one photon exciting two atoms effect. However, the spin-spin interaction, that is not considered in Ref. 30, reduces the dressing. When ε_1 and ε_2 are both negative, the system states are decoupled with respect to the longitudinal interaction if $M = m_1 - m_2 = 0$. This occurs when $m_1 = m_2 = \pm 1$, so when the atoms are both either in the ground $|gg\rangle$ or in the excited $|ee\rangle$ states. However, the transverse interactions still affect our system generating a small dressing that reduces the projection $P_{gg1}^{(4)}$ and $P_{ee0}^{(3)}$ to almost 0.8 at $\varepsilon_1/2\pi = -2.4$ GHz.

Discussion

We measured the spectrum of a circuit composed of two artificial atoms ultrastrongly coupled to a LC resonator. The generalized Dicke Hamiltonian with spin-spin interaction describes well the measured spectrum. At the energy where the sum of the atomic energies al-

most matches the one of the resonator, we observed one anticrossing between the states $|gg1\rangle$ and $|ee0\rangle$. This experimentally confirms the recent theoretical prediction that one-photon can simultaneously excites two atoms [30], opening a new chapter in quantum nonlinear optics.

Future work would involve reading out the qubit and photon states [45] as well as observing the one photon exciting two atoms dynamics. These studies could also

be extended to explore, for example, photon down- and up-conversion [29] and ultrafast two qubit gates [14, 17].

Data availability

The data that support the findings of this study are available from the corresponding authors upon reasonable request.

-
- [1] Y. Nakamura *et al.*, Coherent control of macroscopic quantum states in a single-Cooper-pair box, *Nature* **398**, 786 (1999).
- [2] X. Gu *et al.*, Microwave photonics with superconducting quantum circuits, *Physics Reports* **718-719**, 1 (2017).
- [3] P. Krantz *et al.*, A quantum engineer’s guide to superconducting qubits, *Applied Physics Reviews* **6**, 021318 (2019).
- [4] M. Kjaergaard *et al.*, Superconducting Qubits: Current State of Play, *Annual Review of Condensed Matter Physics* **11**, 369 (2020).
- [5] A. Blais *et al.*, Circuit quantum electrodynamics, *Reviews of Modern Physics* **93**, 025005 (2021).
- [6] S. Kwon *et al.*, Gate-based superconducting quantum computing, *Journal of Applied Physics* **129**, 041102 (2021).
- [7] T. Niemczyk *et al.*, Circuit quantum electrodynamics in the ultrastrong-coupling regime, *Nature Physics* **6**, 772 (2010).
- [8] F. Yoshihara *et al.*, Superconducting qubit–oscillator circuit beyond the ultrastrong-coupling regime, *Nature Physics* **13**, 44 (2017).
- [9] P. Forn-Díaz *et al.*, Ultrastrong coupling of a single artificial atom to an electromagnetic continuum in the non-perturbative regime, *Nature Physics* **13**, 39 (2017).
- [10] S. J. Bosman *et al.*, Multi-mode ultra-strong coupling in circuit quantum electrodynamics, *npj Quantum Information* **3**, 1 (2017).
- [11] Z. Ao *et al.*, Extremely large Lamb shift in a deep-strongly coupled circuit QED system with a multimode resonator, *Scientific Reports* **13**, 11340 (2023).
- [12] A. Frisk Kockum *et al.*, Ultrastrong coupling between light and matter, *Nature Reviews Physics* **1**, 19 (2019).
- [13] P. Forn-Díaz *et al.*, Ultrastrong coupling regimes of light-matter interaction, *Reviews of Modern Physics* **91**, 025005 (2019).
- [14] G. Romero *et al.*, Ultrafast Quantum Gates in Circuit QED, *Physical Review Letters* **108**, 120501 (2012).
- [15] T. H. Kyaw *et al.*, Creation of quantum error correcting codes in the ultrastrong coupling regime, *Physical Review B* **91**, 064503 (2015).
- [16] Y. Wang *et al.*, Holonomic quantum computation in the ultrastrong-coupling regime of circuit QED, *Physical Review A* **94**, 012328 (2016).
- [17] Y. Wang *et al.*, Ultrafast quantum computation in ultrastrongly coupled circuit QED systems, *Scientific Reports* **7**, 44251 (2017).
- [18] R. Stassi *et al.*, Scalable quantum computer with superconducting circuits in the ultrastrong coupling regime, *npj Quantum Information* **6**, 1 (2020).
- [19] Y.-H. Chen *et al.*, Fast binomial-code holonomic quantum computation with ultrastrong light-matter coupling, *Physical Review Research* **3**, 033275 (2021).
- [20] S. D. Liberato *et al.*, Quantum vacuum radiation spectra from a semiconductor microcavity with a time-modulated vacuum Rabi frequency, *Physical Review Letters* **98**, 103602.
- [21] S. Ashhab and F. Nori, Qubit-oscillator systems in the ultrastrong-coupling regime and their potential for preparing nonclassical states, *Physical Review A* **81**, 042311 (2010).
- [22] R. Stassi *et al.*, Spontaneous Conversion from Virtual to Real Photons in the Ultrastrong-Coupling Regime, *Physical Review Letters* **110**, 243601 (2013).
- [23] M. Cirio *et al.*, Ground State Electroluminescence, *Physical Review Letters* **116**, 113601 (2016).
- [24] R. Stassi *et al.*, Unveiling and veiling an entangled light-matter quantum state from the vacuum, *Physical Review Research* **5**, 043095 (2023).
- [25] S.-P. Wang *et al.*, Probing the symmetry breaking of a light–matter system by an ancillary qubit, *Nature Communications* **14**, 4397 (2023).
- [26] L. Garziano *et al.*, Vacuum-induced symmetry breaking in a superconducting quantum circuit, *Physical Review A* **90**, 043817 (2014).
- [27] L. Garziano *et al.*, Multiphoton quantum Rabi oscillations in ultrastrong cavity QED, *Physical Review A* **92**, 063830 (2015).
- [28] R. Stassi *et al.*, Quantum nonlinear optics without photons, *Physical Review A* **96**, 023818 (2017).
- [29] A. F. Kockum *et al.*, Deterministic quantum nonlinear optics with single atoms and virtual photons, *Physical Review A* **95**, 063849 (2017).
- [30] L. Garziano *et al.*, One Photon Can Simultaneously Excite Two or More Atoms, *Physical Review Letters* **117**, 043601 (2016).
- [31] P. Ball, Two Atoms Can Jointly Absorb One Photon, *Physics* **9**, 83 (2016).
- [32] P. T. C. So *et al.*, Two-photon excitation fluorescence microscopy, *Annual Review of Biomedical Engineering* **2**, 399 (2000).
- [33] W. Denk *et al.*, Two-Photon Laser Scanning Fluorescence Microscopy, *Science* **248**, 73 (1990).
- [34] T. Miyanaga *et al.*, Ultrastrong Tunable Coupler Between Superconducting *LC* Resonators, *Physical Review Applied* **16**, 064041 (2021).
- [35] J. Zotova *et al.*, Compact Superconducting Microwave Resonators Based on Al – AlO_x – Al Capacitors, *Physical Review Applied* **19**, 044067 (2023).

- [36] I. Chiorescu *et al.*, Coherent dynamics of a flux qubit coupled to a harmonic oscillator, *Nature* **431**, 159 (2004).
- [37] A. Tomonaga *et al.*, Quasiparticle tunneling and $1/f$ charge noise in ultrastrongly coupled superconducting qubit and resonator, *Physical Review B* **104**, 224509 (2021).
- [38] P.-M. Billangeon *et al.*, Circuit-QED-based scalable architectures for quantum information processing with superconducting qubits, *Physical Review B* **91**, 094517 (2015).
- [39] T. L. Robertson *et al.*, Quantum theory of three-junction flux qubit with non-negligible loop inductance: Towards scalability, *Physical Review B* **73**, 174526 (2006).
- [40] F. Yoshihara *et al.*, Hamiltonian of a flux qubit-LC oscillator circuit in the deep-strong-coupling regime, *Scientific Reports* **12**, 6764 (2022).
- [41] L.-H. Du *et al.*, Generalized Rabi model in quantum-information processing including the \vec{A}^2 term, *Physical Review A* **86**, 014303 (2012).
- [42] J. R. Johansson *et al.*, QuTiP: An open-source python framework for the dynamics of open quantum systems, *Computer Physics Communications* **183**, 1760 (2012).
- [43] J. R. Johansson *et al.*, QuTiP 2: A python framework for the dynamics of open quantum systems, *Computer Physics Communications* **184**, 1234 (2013).
- [44] T. Jaako *et al.*, Ultrastrong-coupling phenomena beyond the Dicke model, *Physical Review A* **94**, 033850 (2016).
- [45] S. Felicetti *et al.*, Parity-dependent State Engineering and Tomography in the ultrastrong coupling regime, *Scientific Reports* **5**, 11818 (2015).
- [46] Y. Sato *et al.*, Three-dimensional multi-scale line filter for segmentation and visualization of curvilinear structures in medical images, *Medical Image Analysis* **2**, 143 (1998).
- [47] S. v. d. Walt *et al.*, scikit-image: image processing in Python, *PeerJ* **2**, e453 (2014).

Acknowledgements

We thank Y. Zhou, R. Wang, and S. Kwon for their thoughtful comments on this research. This paper was based on results obtained from JSPS KAKENHI (Grant Number JP 22K21294) and a project, JPNP16007, commissioned by the New Energy and Industrial Technology Development Organization (NEDO), Japan. Supporting from JST CREST (Grant No. JPMJCR1676) and Moonshot R&D (Grant No. JPMJMS2067) is also appreciated. R.S. acknowledges the Army Research Office (ARO) (Grant No. W911NF1910065). F.N. is supported in part by: Nippon Telegraph and Telephone Corporation (NTT) Research, the Japan Science and Technology Agency (JST) [via the Quantum Leap Flagship Program (Q-LEAP)], and the Moonshot R&D Grant Number JPMJMS2061], the Asian Office of Aerospace Research and Development (AOARD) (via Grant No. FA2386-20-1-4069), and the office of Naval Research (ONR).

Author contributions

A.T. designed the device, carried out the experiment and analyzed the data. A.T. and R.S. performed theoretical and numerical calculations. H.M. carried out part of the experiment. All the authors participated in the discussions and wrote and contributed to editing the manuscript.

Appendix A. Circuit Hamiltonian

Here we describe the circuit Hamiltonian calculation in detail. The branch fluxes across the circuit elements, which are junctions, the inductance L_r , and the capacitance C_r , follow Kirchhoff's voltage laws:

$$\varphi_{\beta 1} + \varphi_{\alpha 1} + \varphi_{a 1} + \varphi_{b 1} = \varphi_{e 1}, \quad (\text{A1})$$

$$\varphi_{\beta 2} + \varphi_{\alpha 2} + \varphi_{a 2} + \varphi_{b 2} = \varphi_{e 2}, \quad (\text{A2})$$

$$\varphi_{c r} + \varphi_{l r} + \varphi_{\beta 1} - \varphi_{\beta 2} = 0, \quad (\text{A3})$$

where $\varphi_{c r}$ and $\varphi_{l r}$ represent fluxes between the resonator capacitor and the inductor. The total Lagrangian of the circuit is described as the summation of circuit components as

$$\mathcal{L}_{\text{tot}} = \mathcal{K}_{J1} + \mathcal{K}_{J2} - \mathcal{U}_{J1} - \mathcal{U}_{J2} + \mathcal{L}_r, \quad (\text{A4})$$

where

$$\mathcal{K}_{Jk} = \frac{C_J}{2} \left[\beta \dot{\phi}_{\beta k}^2 + \dot{\phi}_{a k}^2 + \dot{\phi}_{b k}^2 + \alpha_i (\dot{\phi}_{\beta k} + \dot{\phi}_{a k} + \dot{\phi}_{b k})^2 \right], \quad (\text{A5})$$

$$\mathcal{U}_{Jk} = -E_J [\beta_i \cos(\varphi_{\beta k}) + \cos(\varphi_{a k}) + \cos(\varphi_{b k}) + \alpha_i \cos(\varphi_{e k} - \varphi_{\beta k} - \varphi_{a k} - \varphi_{b k})], \quad (\text{A6})$$

$$\mathcal{L}_r = \frac{C_r}{2} \dot{\phi}_{c r}^2 - \frac{1}{2L_r} (\phi_{c r} + \phi_{\beta 1} - \phi_{\beta 2})^2, \quad (\text{A7})$$

and $k \in \{1, 2\}$ represents the index of a qubit. The sub-index cr refers to the capacitor of the resonator. The qubit kinetic energy part of the Lagrangian in Eq. (A4) becomes

$$\mathcal{K}_{Ji} = \frac{1}{2} \dot{\boldsymbol{\Phi}}^T \mathbf{M} \dot{\boldsymbol{\Phi}}, \quad (\text{A8})$$

where $\boldsymbol{\Phi}_k \equiv (\phi_{\beta k} \ \phi_{a k} \ \phi_{b k})^T$ and the mass matrix is given by

$$\mathbf{M}_k = C_J \begin{pmatrix} \beta_k + \alpha_k & \alpha_k & \alpha_k \\ \alpha_k & 1 + \alpha_k & \alpha_k \\ \alpha_k & \alpha_k & 1 + \alpha_k \end{pmatrix}. \quad (\text{A9})$$

Using the canonical conjugate $q_i = \partial \mathcal{L}_{\text{tot}} / \partial \dot{\phi}_i$ for $\dot{\phi}_i$, where $i \in \{\beta_k, a_k, b_k\}$, we can rewrite Eq. (A8) as

$$\mathcal{K}_{Jk} = \frac{1}{2} \mathbf{q}_k^T \mathbf{M}^{-1} \mathbf{q}_k. \quad (\text{A10})$$

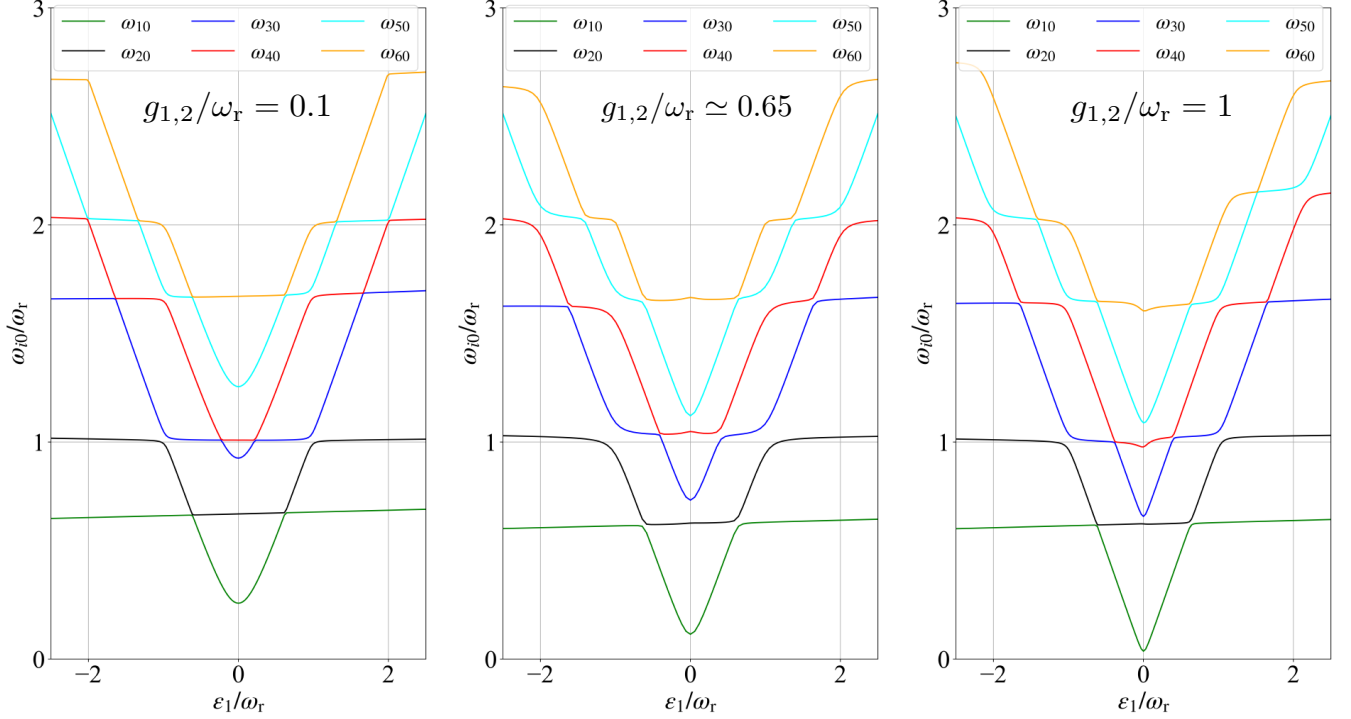


FIG. A1. Frequency difference ω_{i0} for the lowest-energy eigenstates of Hamiltonian Eq. (C1) using different coupling ratio $g_{1,2}/\omega_r \simeq 0, 0.65$ (fitted value), and 1. Other parameters for Eq. (C1) are obtained from fitting the spectrum Fig. 2 The tilt in the horizontal axis originates from the fitting parameter A caused mainly by crosstalk.

Then, we obtain the total Hamiltonian of the circuit as

$$\begin{aligned} \mathcal{H}_{\text{tot}} &= \sum_k \mathbf{q}_k^T \dot{\boldsymbol{\phi}}_k - \mathcal{L}_{\text{tot}} \\ &= \sum_k (4E_c \tilde{\mathbf{q}}_k^T \tilde{\mathbf{M}}_k^{-1} \tilde{\mathbf{q}}_k + E_{\text{Lr}} \varphi_{\beta k}^2 + \mathcal{U}_{Jk}) \\ &\quad + \mathcal{H}_r + \mathcal{H}_{\text{int}}, \end{aligned} \quad (\text{A11})$$

where $2e\tilde{q} = q$ and $C_J \tilde{\mathbf{M}} = \mathbf{M}$, and the term $E_{\text{Lr}} \varphi_{\beta k}$ originates from Eq. (A7) because we define

$$\mathcal{H}_r \equiv \frac{C_r}{2} \phi_{\text{cr}}^2 + \frac{1}{2L_r} \phi_{\text{cr}}^2, \quad (\text{A12})$$

as a bare LC resonator. We expand the total Hamiltonian Eq. (A11) using the eigenvectors $|i\rangle_k$ ($i \in \mathbb{N}$) of the atom Hamiltonians ($\mathcal{H}_{\text{tot}} - \mathcal{H}_r - \mathcal{H}_{\text{int}}$),

$$\begin{aligned} \hat{\mathcal{H}}_{\text{tot}} &= \hbar \sum_i (\Omega_i^{(1)} |i\rangle_1 \langle i|_1 + \Omega_i^{(2)} |i\rangle_2 \langle i|_2) + \hat{\mathcal{H}}_r \\ &\quad - \hbar \sum_{i,j} (g_{ij}^{(1)} |i\rangle_1 \langle j|_1 - g_{ij}^{(2)} |i\rangle_2 \langle j|_2) (\hat{a}^\dagger + \hat{a}) \\ &\quad - E_L \sum_{i,j} g_{ij}^{(1)} g_{ij}^{(2)} |i\rangle_1 \langle i|_2 \langle j|_1 \langle j|_2, \end{aligned} \quad (\text{A13})$$

where $\hbar\Omega_i^{(k)}$ is the i -th eigenenergy of atom k and $\hbar g_{ij}^{(k)} = I_{z\text{pf}} \Phi_0 \langle i | \hat{\varphi}_{\beta k} | j \rangle$ is the coupling matrix element ($I_{z\text{pf}} =$

$\sqrt{\hbar\omega_r/2L_r}$). When we use the two lowest eigenstates for each qubit, we can obtain the Hamiltonian with the two-level system qubits and the N -level system resonator as shown in Eqs. (5) and (6). In Eqs. (5) and (6), the spin-spin interaction reduces the current flowing in the resonator loop, which in this system is the ferromagnetic coupling.

For the fitting, we use Eq. (6), and 11 fitting parameters, this includes the offset value when $\varepsilon_1 = 0$ and the persistent current I_{p1} in qubit 1 to derive $\varepsilon_1 = I_{p1} \Phi_0 (\varphi_{e1} - 0.5)$, where Φ_0 is the flux quantum. We also use the photo-processing technique to obtain peak points from the spectrum [37, 46, 47].

Appendix B. Asymmetric spectrum in the generalized Dicke Hamiltonian

Consider the system Hamiltonian [Eq. (6)] with $\Delta_k = 0$, $g_1 = g_2 = g$, and substituting σ_{zk} with its eigenvalue $m_k = \pm 1$, we can write:

$$\mathcal{H}_s/\hbar = \frac{|\varepsilon_1|}{2} m_1 + \frac{|\varepsilon_2|}{2} m_2 + \omega_r a^\dagger a + gM(a^\dagger + a), \quad (\text{B1})$$

with $M = \text{sgn}(\varepsilon_2)m_2 - \text{sgn}(\varepsilon_1)m_1$. Performing the substitution $\hat{a} = \hat{b} - Mg/\omega_r$ in Eq. C4,

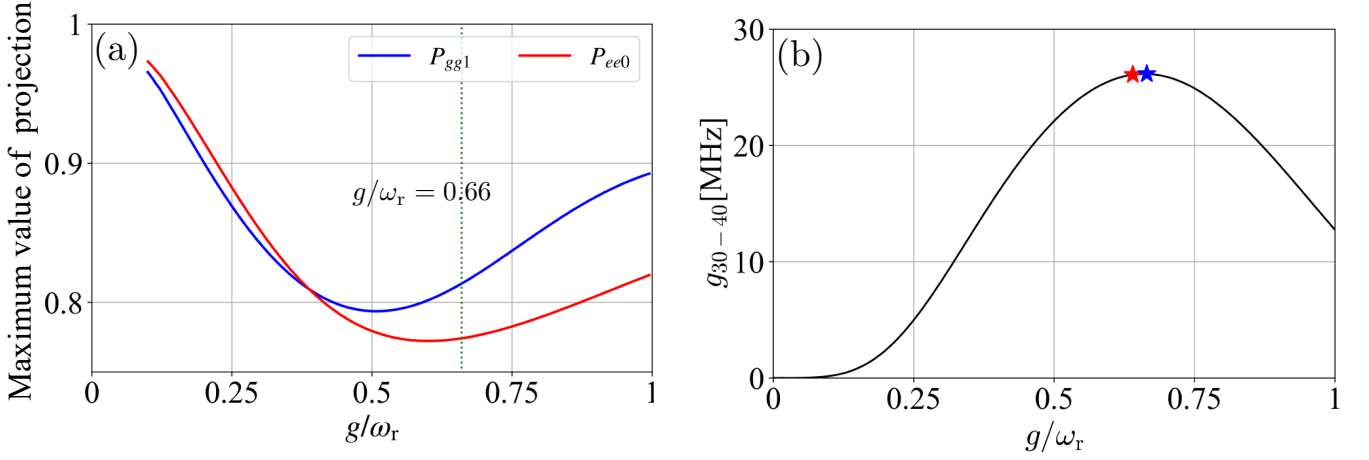


FIG. A2. The left panel shows the maximum value of the projections $P_{gg1}(g/\omega_r)$ and $P_{ee0}(g/\omega_r)$ at the antisplitting point. The green dotted vertical line corresponds to the value that maximizes g_{30-40} . The right panel shows the effective coupling constant g_{30-40} plotted against the coupling ratio g/ω_r . The red and blue star represent $g_1/\omega_r = 0.64$ and $g_2/\omega_r = 0.67$, respectively.

$$\begin{aligned} \mathcal{H}_s/\hbar &= \frac{|\varepsilon_1|}{2}m_1 + \frac{|\varepsilon_2|}{2}m_2 \\ &+ \omega_r(\hat{b}^\dagger - M\frac{g}{\omega_r})(\hat{b} - M\frac{g}{\omega_r}) \\ &+ gM(\hat{b}^\dagger - M\frac{g}{\omega_r} + \hat{b} - M\frac{g}{\omega_r}), \end{aligned} \quad (\text{B2})$$

$$= \omega_r \hat{b}^\dagger \hat{b} + \frac{|\varepsilon_1|}{2}m_1 + \frac{|\varepsilon_2|}{2}m_2 - M^2 \frac{g^2}{\omega_r}, \quad (\text{B3})$$

we obtain the Hamiltonian of a harmonic oscillator. By applying the annihilation operator \hat{b} to its ground state $|0\rangle_M$ (i.e. $\hat{b}|0\rangle_M = 0$), we thus obtain

$$\hat{a}|0\rangle_M = -M\frac{g}{\omega_r}|0\rangle_M. \quad (\text{B4})$$

From Eq. B4, we see that atomic states with $M = 0$ are associated with the zero-photon state; while atomic states with $M = \pm 2$ are associated with the photonic coherent states $|\pm\alpha\rangle$. In turn, M depends on the sign of ε_1 and ε_2 . If $\varepsilon_1 < 0$ and $\varepsilon_2 < 0$, then $M_- \equiv M = m_1 - m_2$. If $\varepsilon_1 > 0$ and $\varepsilon_2 < 0$, then $M_+ \equiv M = -(m_1 + m_2)$. Table I shows the eight possible states as a function of the sign of ε_1 when the interaction is longitudinal. This explains the asymmetry of the spectra respect the sign of ε_1 .

Appendix C. Coupling ratio dependence of one photon exciting two atoms

Figure A1 shows the numerically calculated transition frequency ω_{i0} (spectrum) for the coupling ratios $g_{1,2}/\omega_r = 0, 0.65$ (fitted value), and 1. We use the same

TABLE I. Possible values of M and relative states. We consider $\varepsilon_2 < 0$.

m_1	-1	+1	-1	+1
m_2	-1	-1	+1	+1
M_-	0	+2	-2	0
States if $\varepsilon_1 < 0$	$ gg\rangle 0\rangle$	$ eg\rangle -\alpha\rangle$	$ ge\rangle +\alpha\rangle$	$ ee\rangle 0\rangle$
M_+	+2	0	0	-2
States if $\varepsilon_1 > 0$	$ gg\rangle +\alpha\rangle$	$ eg\rangle 0\rangle$	$ ge\rangle 0\rangle$	$ ee\rangle -\alpha\rangle$

Hamiltonian in Eq. (6),

$$\begin{aligned} \hat{\mathcal{H}}_{\text{tot}}/\hbar &\simeq \omega_r \hat{a}^\dagger \hat{a} \\ &+ \frac{\varepsilon_1}{2}\hat{\sigma}_{z1} + \frac{\Delta_1}{2}\hat{\sigma}_{x1} + \frac{\varepsilon_2}{2}\hat{\sigma}_{z2} + \frac{\Delta_2}{2}\hat{\sigma}_{x2} \\ &- (g_1\hat{\sigma}_{z1} - g_2\hat{\sigma}_{z2})(\hat{a}^\dagger + \hat{a}) - \frac{2g_1g_2}{\omega_r}\hat{\sigma}_{z1}\hat{\sigma}_{z2}, \end{aligned} \quad (\text{C1})$$

and fitting parameters. We can see that the asymmetry of the spectrum increases with $g_{1,2}/\omega_r$, and the antisplitting gap between ω_{30} and ω_{40} in $g_{1,2}/\omega_r \simeq 0.65$ ($-1 < \varepsilon_1/\omega_r < 0$) is larger than that of the other two coupling ratios.

We numerically calculate the projection $P_j \equiv |\langle \Psi_j | j \rangle|^2$

of the superposition states,

$$|\Psi_{gg1}\rangle \simeq (|\psi_3\rangle + |\psi_4\rangle)/\sqrt{2} (\simeq |gg1\rangle), \quad (\text{C2})$$

$$|\Psi_{ee0}\rangle \simeq (|\psi_3\rangle - |\psi_4\rangle)/\sqrt{2} (\simeq |ee0\rangle), \quad (\text{C3})$$

at the anticrossing point on the bare states $|j\rangle = \{|gg1\rangle, |ee0\rangle\}$ as a function of the coupling ratio, and the result is shown in Fig. A2(a). As mentioned in the theoretical prediction in Ref. 30, a lower g/ω_r maximizes the projection. However, the effective coupling strength below $g/\omega_r = 0.1$ is much smaller than that at larger coupling ratios, see Fig. A2(b). Thus, when g/ω_r is below 0.1, we cannot clearly see the antisplitting between $|gg1\rangle$ and $|ee0\rangle$ and the one photon exciting two atoms effect. As shown in the right panel of Fig. A2, the effective coupling is maximum at around $g_{1,2}/\omega_r \simeq 0.66$, which is close to our system.

According to the theoretical prediction in Ref. 30, when the Hamiltonian has no direct spin-spin interac-

tion, which is written as

$$\begin{aligned} \mathcal{H}_{\text{ideal}}/\hbar = & \frac{\omega_q}{2} \sum_{i=1,2} \hat{\sigma}_{zi} + \omega_r a^\dagger a \\ & + g \sum_{i=1,2} (\hat{\sigma}_{zi} \cos \theta + \hat{\sigma}_{xi} \sin \theta)(\hat{a}^\dagger + \hat{a}), \end{aligned} \quad (\text{C4})$$

the effective coupling strength Ω between $|gg1\rangle$ and $|ee0\rangle$ can be approximate to

$$\Omega \simeq \frac{8}{3} \frac{g^3}{\omega_q^2} \sin \theta \cos \theta^2, \quad (\text{C5})$$

where ω_q is the qubit frequency, and $\theta = \arctan(-\Delta/\varepsilon)$. The parameters in our system are $\theta_1 \simeq 0.09 \times 2\pi$, $\theta_2 \simeq 0.06 \times 2\pi$, $\omega_{q1} \simeq 3.42$ GHz, and $\omega_{q2} \simeq 2.48$ GHz. From Eq. (C5), the effective coupling constant Ω obtained using the parameters in our system is expected to be more than 200 MHz. The measured effective coupling constant g_{30-40} is much suppressed. Besides, if the Hamiltonian has no direct spin-spin interaction, the projections on $|gg1\rangle$ and $|ee0\rangle$ at the anticrossing point is less than 0.8 when $g/\omega_r = 0.25$, and when $g/\omega_r \gg 0.25$, the one photon exciting two atoms effect is no longer observed.